Computational Methods in Engineering and Science, Iu et al. (eds)
© 2003 Swets & Zeitlinger, Lisse, ISBN 90 5809 567 3

Numerical modeling of metal forming – current practice and advanced applications

S. Cescotto, L. Duchêne, F. Pascon & A.M. Habraken
M&S Dep., University of Liège, Belgium

ABSTRACT: This paper first summarizes the current possibilities and the perspectives of effective modeling of metal forming processes. Practical considerations on manpower requirement and data availability are included in the discussion. Then, two examples of advanced applications are presented: the micro-macro approach for the modeling of sheet metal forming and the modeling of continuous casting.

1 CURRENT POSSIBILITIES AND PERSPECTIVES OF METALFORMING MODELING

1.1 *Introduction*

Nowadays, the specifications in terms of product quality and production time are such that modeling the metal forming of industrial parts has become compulsory. A large number of research and commercial computer codes are available and it is not always easy to make a choice among them. Hereafter, a few practical guidelines are proposed.

1.2 *General scheme of computer modeling*

Modeling must be considered as a set of operations including pre-processing, calculations, post-processing and optimization loop (Fig. 1).

Pre-processing consists in the definition of the data set. User friendliness is essential. One should merely specify the process parameters (tools used such as hydraulic press, drop hammer, etc; initial temperatures of dies and workpiece, reference numbers for the geometry of dies and workpiece which are independently defined in the CAD data base) and the material data including contact conditions (thermo-mechanical properties, friction coefficient, ...).

The finite element software is the core of the modeling: 2D and 3D analyses are possible. Today, automatic remeshing is fully available in 2D but there still remains to improve 3D remeshing in terms of robustness and computer time. In any case, 3D finite element simulation of the forming of complex industrial parts is time consuming. Parallel computation is normally required.

Post processing is, in most cases, the presentation of the finite element results in an attractive and easy-to-read way on which basis the user takes the decision to validate the process if the specifications are met or to modify it if necessary. Modifications are usually based on the experience of the user and are followed by a new finite element simulation. However, the automatic improvement the process parameters is sometimes available thanks to optimization techniques. So far, this is seldom proposed by general purpose commercial codes because optimization is closely linked with the particularities of the considered forming process, but intensive research work is currently performed in this direction.

1.3 *Material data*

Two aspects deserve careful attention: the type of constitutive model and the acquisition of material data: the more sophisticated the model, the more difficult the determination of the corresponding parameters. Table 1 lists some classical types of metal models.

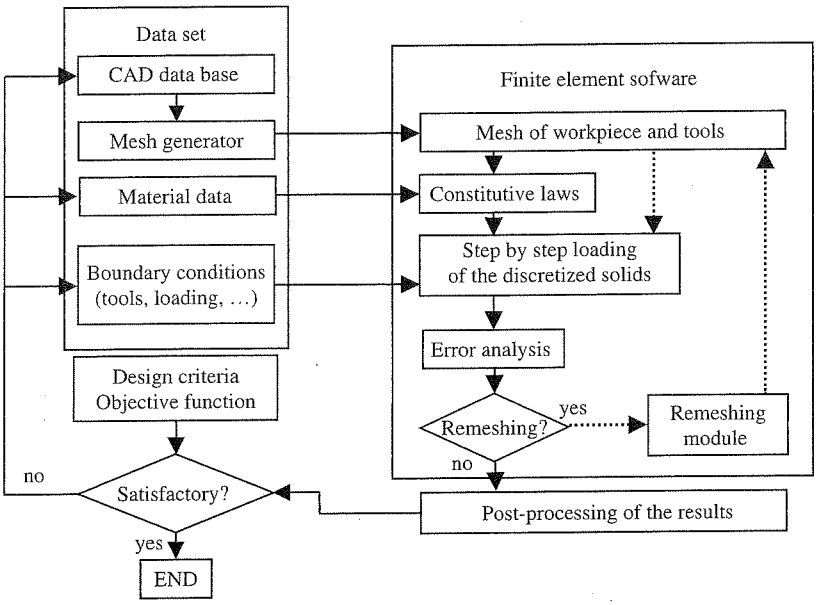

Figure 1. General scheme of metal forming modeling.

Table 1. Material models and corresponding potential results.

Model	Potential results
1. Rigid plastic	Cold bulk forming, shape of workpiece, stresses and strains distribution except at the end of closed die forging
2. Elasto-plastic	Same as 1plus stresses and strains distribution at the end of closed die forging and elastic springback
3. Rigid-visco-plastic	Same as 1 but applicable to hot forming, average temperature is considered
4. Elastic-visco-plastic	Same as 2 but applicable to hot forming, average temperature is considered
5. Thermo-visco-plastic (rigid or elastic)	Same as (rigid or elastic)-visco-plastic but the detailed distribution of temperature is considered
6. Damage	Can be combined with preceding models, damage distribution and fracture initiation can be predicted
7. Isotropic	Usually sufficient for bulk forming
8. Anisotropic	Necessary for sheet metal forming, models can be macro or micro; anisotropy can be considered for elastic, plastic and/or damage behaviors
9. Micro-macro	Macroscopic behavior (elastic, plastic, ...) deduced from behavior of crystals by some averaging technique; important for sheet metal forming
10. Recrystallization	Can be combined with thermo-(visco)-plastic models, grain size and recrystallized zones can be predicted
11. Phase changes	Important for cooling processes (continuous casting), heat treatment, ...
12. Contact	Coulomb's friction law or more advanced models

So, the constitutive model must be chosen according to the precision expected from the simulation. For models 1, 2, 3 and for usual metals, data tables are available as in Altan, Oh, Gegel (1983) or on the web (e.g. www.matweb.com), but for particular alloys, experiments are necessary. In addition, the validity of available data is sometimes questionable. For example, the scatter of literature data on Young's modulus at high temperature is important, as illustrated by Figure 2. For more complex models, data acquisition often requires expensive and time consuming laboratory tests. For example in the visco-plastic domain, Norton-Hoff law is widely used. Its identification requires compression or torsion tests at high temperature,

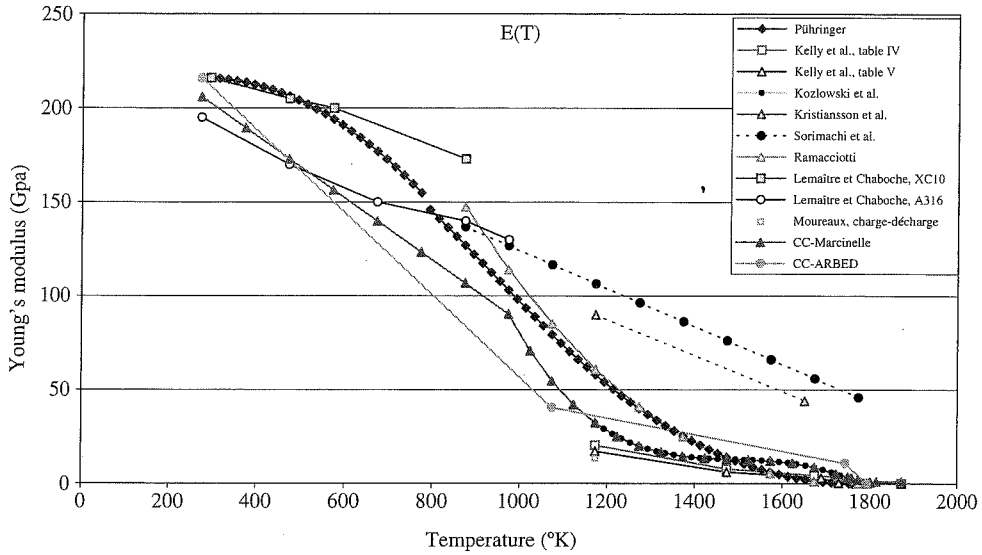

Figure 2. Young's modulus of steel as a function of temperature from different data sources.

using non classical equipment at least at 3 temperatures and 3 strain rates. It takes about 1 week to get the results. An extreme case is encountered when metallurgical phase changes must be taken into account: getting all the necessary data for a new metal could take a few years in the worst cases!

For the micro-macro approach, which is well developing for the modeling of sheet metal forming, it is necessary to know on the one hand, the slip planes and the corresponding critical resolved shear stresses as well as the twinning modes of the crystal, and, on the other hand, the ODF (Orientation Distribution Function) of the metal sheet, which can be obtained by X-ray or neutron diffraction.

1.4 *Conclusion*

From the industrial point of view, when purchasing a computer code to model metal forming processes, it is vital to check the adequacy of the available material models and data with the types of metals used and the process conditions. The cost and time of data acquisition must be taken into account as an essential factor of the purchase decision.

2 ADVANCED MODELING OF SHEET METAL FORMING

2.1 *Introduction*

The goal is to integrate the influence of material texture in sheet metal forming simulations. The constitutive law describing the mechanical behavior is based on a microscopic approach at the crystallographic level. A large number of crystals must be used to represent correctly the global behavior. The transition from crystal level to macroscopic level is based on the full constraint Taylor's model. This model does not lead to a general law with a mathematical formulation of the yield locus. Only one point of the yield locus corresponding to a particular strain rate direction can be computed. To obtain such a stress point, it is assumed that the macroscopic stress results from the average of the microscopic stresses in each crystal belonging to a set of representative crystals, the orientations of which approximate the actual texture of the material. Repeating this for a large number of strain rate directions generates a set of stress points belonging to the yield surface in stress space. Fitting an equation on this set provides the analytical expression of the yield surface. For example, a least square fitting of a 6th order series (210 coefficients) on a large number of stress points (typically 70300) in the deviatoric stress space has been adopted by Munhoven et al. 1996. This is a global description of the yield locus that can be implemented in a FEM code. Unfortunately,

taking account of texture evolution would imply the computation of the 210 coefficients of the 6th order series for each integration point, each time texture updating is necessary. This would require an impressive amount of computation and memory storage (210 coefficients for each integration point) which is only partially useful as, generally, for a given material point, the stress state remains in a local zone of the yield locus during the forming process. So, an original approach is investigated in which a direct interpolation between points in strain space and in stress space is achieved. With this method, only a local zone of the yield locus is used at a time for each integration point.

2.2 *Local description of a scaled yield locus*

We work in the 5 dimensional (5D) deviatoric strain and stress spaces. Let $\mathbf{s}^{*0}$ be one unit stress vector, direction of the central point of the local part of the yield locus that requires an approximation. $\mathbf{s}^{*(i)}$ are five unit stress vectors surrounding $\mathbf{s}^{*0}$ and determining the interpolation domain. They will be called the "domain limit vectors". They have the following properties:

- they are unit vectors: $\mathbf{s}^{*(i)} \cdot \mathbf{s}^{*(i)} = 1$ (no sum on i) and $\mathbf{s}^{*0} \cdot \mathbf{s}^{*0} = 1$
- there is a common angle between all $\mathbf{s}^{*(i)}$: $\mathbf{s}^{*(i)} \cdot \mathbf{s}^{*(j)} = 1 + \beta^2(\delta_{ij} - 1)$ i, j = 1 ... 5
- there is a common angle between each $\mathbf{s}^{*(i)}$ and $\mathbf{s}^{*0}$: $\mathbf{s}^{*0} \cdot \mathbf{s}^{*(i)} = \cos\theta$ i, j = 1 ... 5
- they determine a regular domain.

Hence, the central direction $\mathbf{s}^{*0}$ can be computed as a scaled average of the 5 domain limit vectors $\mathbf{s}^{*(i)}$:

$$\mathbf{s}^{*0} = \frac{1}{\cos\theta} \sum_{i=1}^{5} \mathbf{s}^{*(i)} \tag{1}$$

Both θ and β determine the size of the interpolation domain. They are linked by:

$$\beta^2 = \frac{6}{5} \sin^2\theta \tag{2}$$

As the 5 $\mathbf{s}^{*(i)}$ vectors are linearly independent, they constitute a covariant vector basis of the 5-dimensional space. The (non unit) contravariant base vectors are defined by:

$$\mathbf{ss}^{(i)} \cdot \mathbf{s}^{*(j)} = \delta_{ij} \tag{3}$$

and one can check that they depend linearly on vectors $\mathbf{s}^{*(i)}$ and $\mathbf{s}^{*0}$:

$$\mathbf{ss}^{(i)} = \frac{1}{\beta^2} \left(\mathbf{s}^{*(i)} - \frac{1-\beta^2}{\cos\theta} \mathbf{s}^{*0} \right) \tag{4}$$

The 5 η-coordinates of any vector $\mathbf{V} = \sum_{i=1}^{N} \eta_i \mathbf{s}^{*(i)}$ are determined from:

$$\mathbf{V} \cdot \mathbf{ss}^{(j)} = \sum_{i=1}^{N} \eta_i \mathbf{s}^{*(i)} \cdot \mathbf{ss}^{(j)} = \sum_{i=1}^{N} \eta_i \delta_{ij} = \eta_j \tag{5}$$

For a unit vector $\mathbf{V}$ coinciding with a domain limit vector $\mathbf{s}^{*(i)}$, the η-coordinates are:

$$\eta_j = \delta_{ij} \qquad \text{with} \quad j = 1..5 \tag{6}$$

The domain limit vectors represent the domain vertices. The 5 limit boundaries (or edges) of the interpolation domain have the equation: $\eta_i = 0$.

The above choices imply that any point belonging to the interpolation domain is associated to positive η-coordinates.

To determine the 5 domain limit vectors $\mathbf{s}^{*(i)}$, 5 unit vectors $\mathbf{s}'^{*(i)}$, are computed as a linear relation between $\mathbf{s}'^{*0} = <1, 1, 1, 1, 1>$ and successively, each vector of the Cartesian basis $\mathbf{e}^{(i)}$ (for example $\mathbf{e}^{(2)} = <0, 1, 0, 0, 0>$)

$$\mathbf{s}'^{*(i)} = \alpha\, \mathbf{s}'^{*0} + \beta\, \mathbf{e}^{(i)} \quad \text{with} \quad \alpha = \frac{\cos\theta}{5} - \frac{\sin\theta}{2} \quad \text{and} \quad \beta^2 = \frac{5}{4}\sin^2\theta \tag{7}$$

Then the rotation linking the real required central point $\mathbf{s}^{*0}$ and $\mathbf{s}'^{*0}$ is given by:

$$\mathbf{R} = \mathbf{I} + 2\,\mathbf{s}^{*0} \otimes \mathbf{s}'^{*0} - \frac{\left(\mathbf{s}^{*0} + \mathbf{s}'^{*0}\right) \otimes \left(\mathbf{s}^{*0} + \mathbf{s}'^{*0}\right)}{1 + \mathbf{s}^{*0} \cdot \mathbf{s}'^{*0}}, \tag{8}$$

where $\mathbf{I}$ is the second order unit tensor. It provides the domain limit vectors:

$$\mathbf{R} \cdot \mathbf{s}'^{*(i)} = \mathbf{s}^{*(i)} \tag{9}$$

Now, let us consider both 5D stress and strain rate spaces. A regular domain is built in the strain rate space. It is defined by its 5 vertices $\mathbf{u}^{*(i)}$ (unit vectors). Thanks to 5 calls to Taylor's module, the associated stress vectors $\mathbf{s}^{(i)}$ can be defined. These 5 stress vectors define a non-regular domain in the stress space. The contravariant base vectors in each space are

$$\mathbf{uu}^{(i)} \cdot \mathbf{u}^{*(j)} = \delta_{ij} \qquad \text{and} \qquad \mathbf{ss}'^{(i)} \cdot \mathbf{s}^{(j)} = \delta_{ij}\,. \tag{10}$$

The contravariant vectors $\mathbf{ss}'^{(i)}$ computed above and $\mathbf{ss}^{(i)}$ given by (5) differ only because in (5), unit stress directions $\mathbf{s}^{*(i)}$ are used. Here the length of the stress vectors $\mathbf{s}^{(i)}$ is an important characteristic as it defines the yield locus anisotropy. These contravariant vectors $\mathbf{ss}'^{(i)}$ and $\mathbf{uu}^{(i)}$ give, in each space, the η-coordinates associated to any stress $\mathbf{s}$ or unit strain rate $\mathbf{u}^*$: $\eta_i = \mathbf{uu}^{(i)} \cdot \mathbf{u}^*$ and $\eta_i = \mathbf{ss}'^{(i)} \cdot \mathbf{s}$.

So any stress vector $\mathbf{s}$ or strain rate direction $\mathbf{u}^*$ can be represented with the help of the vector basis of their respective space and the η-coordinates:

$$\mathbf{u}^* = \sum_{i=1}^{5} \eta_i\, \mathbf{u}^{*(i)} \quad \text{and} \quad \mathbf{s} = \sum_{i=1}^{5} \eta_i\, \mathbf{s}^{(i)} \tag{11}$$

Physically, a material state corresponds to one stress point $\mathbf{s}$ and one strain rate direction $\mathbf{u}^*$.

As a basic hypothesis, it is assumed that the η-coordinates computed by (11) are equal when the stress $\mathbf{s}$ and the strain rate direction $\mathbf{u}^*$ are physically associated. This property is exactly fulfilled on the domain limit vectors. The stress $\mathbf{s}^{(i)}$ corresponds to the strain rate direction $\mathbf{u}^{*(i)}$ and their η-coordinates are $\eta_i = 1$ and $\eta_j = 0$ ($i \neq j$) in both spaces. This property is extended inside the domains by convenience. The so-called stress–strain interpolation approach directly derives from this hypothesis. It provides the following interpolation relation:

$$\mathbf{s} = \sum_{i=1}^{5} (\mathbf{uu}^{(i)} \cdot \mathbf{u}^*)\mathbf{s}^{(i)} = \mathbf{uu}^{(i)} \otimes \mathbf{s}^{(i)} : \mathbf{u}^* = \mathbf{C} : \mathbf{u}^* \tag{12}$$

For each domain, the $\mathbf{C}$ matrix is computed once from the stress domain limit vectors $\mathbf{s}^{(i)}$ and the contravariant vectors $\mathbf{uu}^{(i)}$ associated to the 5 strain rate vertices $\mathbf{u}^{*(i)}$. Inside one domain, (12) provides the stress state if the strain rate direction is given. The η-coordinates computed for a given $\mathbf{u}^*$ allow to check the domain validity. If any of them does not belong to the interval [0, 1], then the interpolation of (12) becomes an extrapolation and a new local domain is required.

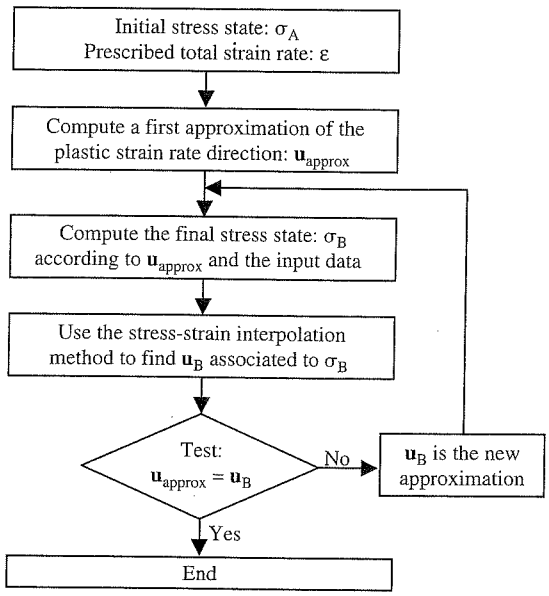

Figure 3. Stress integration scheme.

2.3 *Updating of the scaled yield locus*

When the current local description of the scaled yield locus does not any more cover the interesting zone, one has to find another local description enclosing the interesting part of the yield locus. Of course, the procedure described above could be repeated using one new strain rate direction $\mathbf{u}^*$ as central point. However, looking at the η-coordinate that does not any more belong to [0, 1], one can find the boundary which is not respected by the new explored direction. This boundary is identified by 4 domain limit vectors so that the definition of a new local domain only requires one additional domain limit vector. So, only one new vertex must be computed by Taylor's model to identify the neighbouring domain that probably contains the new explored strain rate direction.

2.4 *Stress integration scheme*

Since the stress–strain interpolation presented above does not use the concept of yield locus in a usual way, a specific integration scheme has been developed. The main ideas are summarized in the diagram of Figure 3 where obviously, no yield locus formulation is used.

At this level, the real stress and not the scaled one is necessary; so the size and the shape of the yield locus cannot any more be dissociated. As (12) only gives the shape corresponding to a reference level of hardening, an additional factor τ is introduced to represent the work hardening by a Swift law:

$$\mathbf{s} = \tau\, \mathbf{C}\,.\mathbf{u}^* \quad \text{with} \quad \tau = K(\Gamma_0 + \Gamma)^n \tag{13}$$

where Γ is the total polycrystal slip. As in Winters 1996, this micro-macro hardening law is identified by a macroscopic uniaxial tensile test.

2.5 *Implementation of the texture updating*

In this model, not only is the texture used to predict the plastic behavior of the material, but the strain history of each integration point is taken into account in order to update the texture. This is summarized in Figure 4. It should be noticed that the constitutive law in the FEM code is based on the interpolation method described earlier and on Taylor's model applied on the actual set of crystallographic orientations through the yield locus. These crystallographic orientations are represented with the help of the Euler

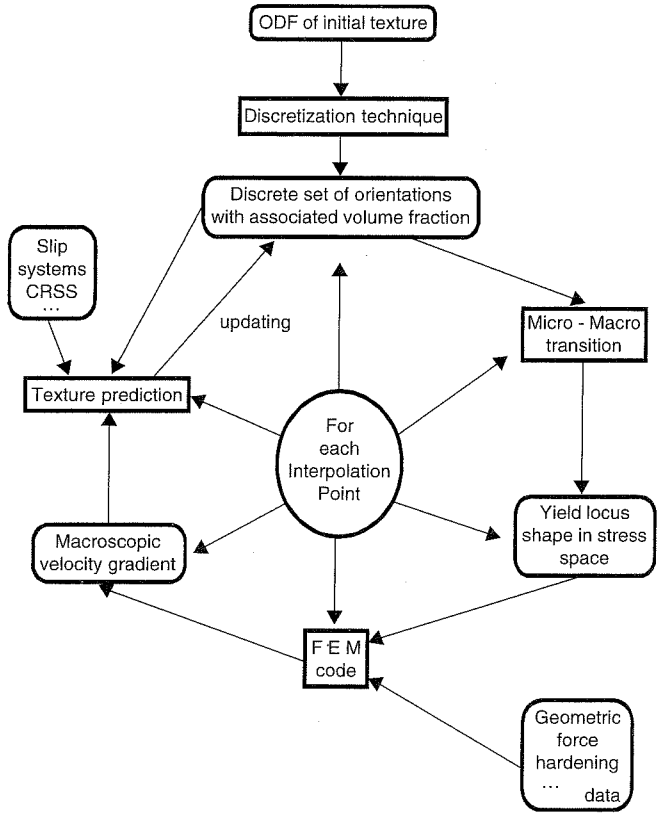

Figure 4. Texture updating.

Table 2. Maximum value of the ODF during deep-drawing.

Steel	Before deep-drawing	After deep-drawing
Mild steel	6	14.34
Dual phase steel	4.12	6.73
Complex phase steel	6.94	8.52

angles, ranging from 0° to 360° for φ_1 and from 0° to 90° for ϕ and φ_2 so as to take crystal cubic symmetry into account.

2.6 *Deep-drawing simulations*

In order to show up the influence of the texture evolution during a forming process, a deep-drawing simulation is examined. Three steels are compared. The first one is a mild steel, the second one is a dual phase steel and the third one is a complex phase steel. Their hardening exponents are respectively 0.2186, 0.2238 and 0.1397. Their tensile yield stresses are 136, 293 and 741 N/mm^2. Their ODF has been measured by X-ray diffraction. The maximum value of this function, i.e. the density of the most represented crystallographic orientation (see Table 2) is an indication of the anisotropy of the studied material.

The geometry of the deep-drawing process consists in a hemispherical punch with a diameter of 100 mm, a die with a curvature radius of 5 mm and a blankholder. The drawing ratio is 1.7; the blankholder force

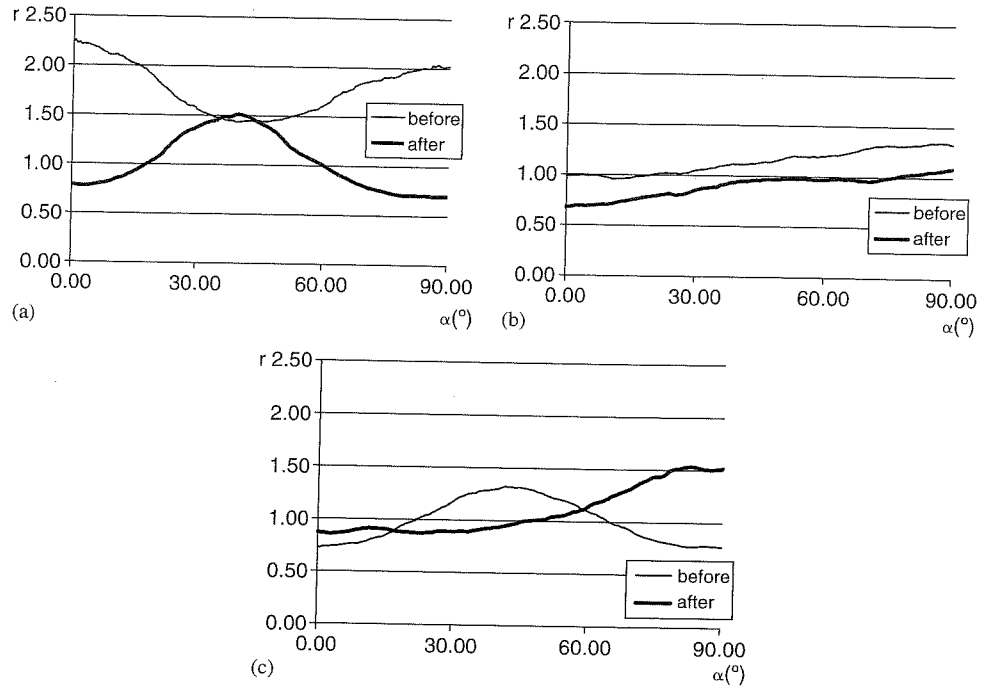

Figure 5. Evolution of the Lankford coefficient "r" for a particular element during the deep drawing process: (a) mild steel (b) dual phase steel (c) complex phase steel.

is 70 kN; the simulation is achieved up to a drawing depth of 50 mm. This geometry has already been used as a benchmark for the NUMISHEET'99 conference. A Coulomb law is used to model friction with a coefficient adapted to each steel. On the finite element mesh, a particular element chosen such that it completely undergoes the drawing process on the curvature of the die is examined. The texture evolution of that element is compared for the three steels. The values of the maximum of the ODF for each steel before and after the process are summarized in Table 2.

The initial anisotropy of the three steels is more or less the same but the behavior of these steels is quite different during deep-drawing, if we focus on the maximum of the ODF (a factor larger than 2 is found at the end of the forming process).

These differences can also be pointed out by the Lankford coefficient "r". This parameter is a good indicator for the drawability of a steel (a high "r" allows larger deep-drawing ratios). Figure 5 shows its evolution during the process. Here again, large differences between the three steels can be noticed. The mild steel is characterised by a high initial r coefficient (inducing a good formability) and a considerable evolution during the simulation. The two other steels have a lower value (around 1.0) and their evolution is also lower. These behaviors are in agreement with the conclusion drawn from the evolution of the maximum of the ODF (see Table 2).

3 ADVANCED MODELING OF CONTINUOUS CASTING

3.1 *Context of the studies*

Continuous casting is widely used nowadays for production of steel all around the world. Although the process has been developed for several decades, research is still needed to continue improving quality and yield. Two different ways are explored: the first one is the optimization of the caster performance, the second one is the management of existing problems in particular casting conditions.

In a first study, a thermo-mechanical F.E.M. model of the steel solidification in the area of the mould was developed, focusing on the effect of the mould taper on the primary cooling in order to optimise the

mould for complex cross sections (beam blanks). Some papers have already been published on this part: see Pascon et al. (2000 & 2001).

In a second time, this model was enhanced to represent the behavior of the steel strand, after the exit of the mould, in the bending as well as in the straightening zone. This study aims at predicting transversal cracking sometimes observed in practice.

3.2 *Macroscopic approach of thermo-mechanical behavior*

3.2.1 *Global approach*

A thermo-mechanical macroscopic model has been worked out using a non-linear finite element code, called LAGAMINE, which has been developed since the early eighties at University of Liege for large strains/displacements problems, more particularly for metal forming modeling.

Since a complete 3D discretization of continuous casting seems difficult to manage (because of numerical stability and convergence reasons, and also because of computation time), a 2D½ model has been preferred.

This model belongs to the "slice models" family. With a 2D mesh, a set of material points representing a slice of the steel strand, perpendicular to the casting direction, is modeled. Initially the slice is at the meniscus level and its temperature is assumed to be uniform and equal to the casting temperature. Since this slice is moving down through the machine, heat transfer, stress and strain development as well as solidification growth are studied according to the boundary conditions imposed by the industrial process.

3.2.2 *Mechanical model*

3.2.2.1 Generalized plane strain state

From a mechanical point of view, the slice is in generalized plane strain state (2D½). That means that the thickness t of the slice is governed by the following equation:

$$t(x,y) = \alpha_0 + \alpha_1 x + \alpha_2 y \tag{14}$$

where α_0, α_1, α_2 are degrees of freedom corresponding respectively to the thickness at the origin of the axes (α_0) and the thickness variations along axes x (α_1) and y (α_2), in the plane of the slice.

This formulation allows the development of stresses and strains in the out-of-plane direction, i.e. in the casting direction. It is thus more complete than classical 2D approaches (plane strain or plane stress states) and much less CPU expensive than a 3D approach.

Moreover, it allows the modeling of bending and straightening of the strand, enforcing a relation between the α_i degrees of freedom so that the correct radius of curvature of the machine is respected.

Last but not least, this 2D½ also permits to apply a force in the casting direction, which is of prime importance since one has to take into account the withdrawal force of the strand due friction in different places in the machine.

3.2.2.2 Constitutive law

The mechanical behavior of steel is modeled by an elastic-viscous-plastic law. The elastic part is governed by a classical Hooke's law. In the viscous-plastic domain, a Norton-Hoff type constitutive law is used, the expression of which (in terms of von Mises equivalent values) is:

$$\bar{\sigma} = \sqrt{3}.p_2.e^{-p_1\bar{\varepsilon}}.(\sqrt{3}.\bar{\dot{\varepsilon}})^{p3}.\bar{\varepsilon}^{p4} \tag{15}$$

where $p_{1,2,3,4}$ are temperature dependent parameters, which can be fit on experimental curves. With the usual assumptions of von Mises yield surface, associated plasticity and normality rule, expression (15) becomes, in tensorial form:

$$\dot{\hat{\varepsilon}}_{ij}^{vp} = \frac{J_2^{p5}.e^{\frac{p_1.\bar{\varepsilon}}{p_3}}.\bar{\varepsilon}^{\frac{p_4}{p_3}}}{2.(K_0.p_2)^{\frac{1}{p_3}}}\cdot\hat{\sigma}_{ij} \tag{16}$$

where $J_2 = \frac{1}{2}\cdot\hat{\sigma}_{ij}\cdot\hat{\sigma}_{ij} = \frac{1}{3}\cdot\bar{\sigma}^2$ and $p_5 = \frac{1-p_3}{2.p_3}$.

The numerical integration of this constitutive law is based on an implicit scheme (see Habraken et al. 1998). All the parameters are thermally affected.

3.2.2.3 Ferrostatic pressure

The liquid pool in the center of the strand applies a pressure on the solidified shell. This pressure is called ferrostatic pressure p_f and it is equal to:

$$p_f = \gamma \cdot D \cdot (1 - f_s) \tag{17}$$

where γ is the volumetric weight of steel, D the depth under the meniscus level and f_s the solid fraction.

Since the studied steel is not a eutectic composition, solidification occurs over a range of temperature limited by the solidus temperature (T_{sol}) and the liquidus one (T_{liq}). A linear variation of the solid fraction according to temperature in this range is assumed:

$$0 \le f_s(T) = \frac{T_{liq} - T}{T_{liq} - T_{sol}} \le 1 \quad \forall T \in \left[T_{liq}, T_{sol}\right] \tag{18}$$

3.2.3 *Thermal aspects*

3.2.3.1 Internal heat conduction

The heat transfer in the material is governed by the classical Fourier's law, expressing the energy conservation and taking into account the release of energy during phase transformation (solidification is exothermic):

$$\frac{\Delta H}{\Delta T}\dot{T} = \nabla \cdot (\lambda \nabla T) \tag{19}$$

where H is the enthalpy, T the temperature and λ the thermal conductivity of the material. The enthalpy H is given by:

$$H = \int \rho \, c \, dT + (1 - f_s).L_F \tag{20}$$

where ρ is the volumetric mass, c the specific heat and L_F the latent heat of fusion.

3.2.3.2 Thermal shrinkage

Thermal shrinkage ε^{therm} due to solidification is given by:

$$\dot{\varepsilon}_{ij}^{therm} = \alpha(T).\dot{T}.\delta_{ij} \tag{21}$$

where α is the linear thermal expansion coefficient, which is thermally affected.

3.2.4 *Boundary conditions*

Different boundary conditions can occur, according to the position of the slice in the machine and to the contact conditions. Table 3 summarizes the different cases:

In case of mechanical contact, the normal pressure is calculated by allowing, but penalizing, the penetration of bodies into each other. The friction τ_c is then computed with Coulomb's friction law:

$$|\tau_c| = \mu.\sigma_n \tag{22}$$

Table 3. Boundary conditions.

Position of the slice in the caster	Contact conditions	Mechanical boundary conditions	Thermal boundary conditions
Primary cooling (slice in the mould)	Contact with the mould	Normal stress + tangential friction	Large heat transfer (direct contact)
	Loss of contact	Free surface (no stress)	Reduced heat transfer (through the slag)
Secondary cooling (under the mould) in the caster	Contact with the rolls	Normal stress + tangential friction	Heat transfer (direct contact with rolls)
	Between the rolls	Free surface (no stress)	Radiation + convection *or* water spray *or* flow

where μ is the friction coefficient and σ_n is the normal stress.

The heat transfer q from the strand to the ambient is given by the simple relation:

$$q = h\left(T_{strand} - T_{ambient}\right) \tag{23}$$

where h is the heat transfer coefficient according to the boundary conditions (see Table 3). In case of contact, h is the inverse of the contact resistance. In case of water spray cooling, h has been experimentally determined for different temperatures (700–1200°C), different shapes of spray, different rates of flow and at different distances from the nozzle.

3.3 *Industrial application*

A first industrial application was the study of the influence of the mould taper on the cooling rate during the primary cooling: it was reported in Pascon et al. (2000 & 2001). Here we want to study the influence of some local defects (such as nozzle perturbation, roll locking or roll misalignment) on the risk of transversal cracks initiation.

To achieve this, two "macroscopic" indicators of crack initiation are defined. Both combine the gap of ductility of steel in a given range of temperature (T_A–T_B for a steel composition) and the mechanical constraints in the direction of casting: the longitudinal stress for the first indicator I_1 and the longitudinal strain rate for the second one I_2.

$$I_1 = \begin{cases} \max\left(\sigma_{zz};0\right) & T \in \left[T_A;T_B\right] \\ 0 & T \notin \left[T_A;T_B\right] \end{cases}$$

$$I_2 = \begin{cases} \max\left(\dot{\varepsilon}_{zz};0\right) & T \in \left[T_A;T_B\right] \\ 0 & T \notin \left[T_A;T_B\right] \end{cases}$$

These indicators are different from zero only if the temperature corresponds to the gap of ductility and if the constraint tends to open a crack (tensile stress or elongation). In such a case, the higher the constraint, the higher the indicators. In any other case, the indicators are equal to zero, what means that the risk of transverse crack initiation vanishes.

The model provides many results, among others: temperature evolution (surface temperature, evolution of solidification, ...), stress and strain states, crack initiation indicators, bulging between rolls, extracting force. Figure 6 represents a part (straightening zone) of the casting of a micro allied steel with standard conditions (without any local defect). This figure shows the value of the 2 indicators and the localization of the maximum values (maximum risk). These results are in agreement with observations on industrial products.

Other computations including local defects (water spray cooling perturbation, roll locking, roll misalignment) have been performed. Comparing the value of the indicators in the reference case (standard conditions) to those of each defect case, we studied the effect of each defect. This comparison allowed us to classify the defects from the less to the most critical.

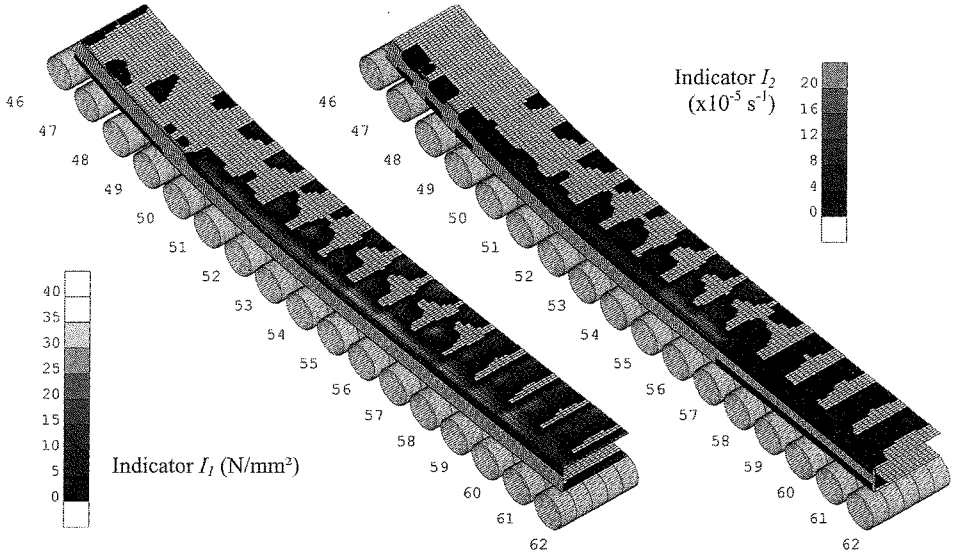

Figure 6. Indicators of risk of transverse crack initiation with standard casting conditions (reconstituted 3D view of the surface of the cast product – ½ structure because of symmetry).

3.4 *Conclusion*

This study shows how powerful is the 2D½ approach: for the complete thermo-mechanical modeling of the strand, the computation time is of the order of 3 to 4 hours on a PC (Pentium) and accurate results are obtained which are confirmed by industrial observations.

ACKNOWLEDGEMENT

Dr. A.-M. Habraken, senior research associate, acknowledges the Belgian National Research Fund for its financial support.

REFERENCES

Altan, Oh, Gegel, 1983. Metal Forming, Fundamentals and Applications

Habraken, A.M., Charles, J.F., Wegria, J. and Cescotto, S. Dynamic Recrystallisation During Zinc Rolling, In: *Int.J. of Forming Processes*, Vol. 1 – n°1 (1998), 53–73

Munhoven, S., Habraken, A. M., Van Bael, A. and Winters, J. 1996. Anisotropic finite element analysis based on texture. *Proc. 3rd Int. Conf.: NUMISHEET'96*: 112–119

Pascon, F., Habraken, A.-M., Bourdouxhe, M. and Labory, F. Modélisation des phénomènes thermo-mécaniques dans une lingotière de coulée continue, In: *Mec. Ind.* Vol. 1 – n°1 (2000), 61–70 (in French)

Pascon, F., Habraken, A.M., Bourdouxhe, M. and Labory, F. Finite element modeling of thermo-mechanical behavior of a steel strand in continuous casting, In: *Proc. 4th ESAFORM Conference*, April 23–25 2001, Liège (Belgium), 867–870

Winters, J. 1996. *Implementation of Texture-Based Yield Locus into an Elastoplastic Finite Element Code.* Ph.D. Thesis, KUL, Leuven